

MOX-Report No. 15/2019

**Hierarchically reduced models for the Stokes problem
in patient-specific artery segments**

Brandes Costa Barbosa, Y. A.; Perotto, S.

MOX, Dipartimento di Matematica
Politecnico di Milano, Via Bonardi 9 - 20133 Milano (Italy)

mox-dmat@polimi.it

<http://mox.polimi.it>

Hierarchically reduced models for the Stokes problem in patient-specific artery segments

Yves Antonio Brandes Costa Barbosa, Simona Perotto

May 14, 2019

MOX– Dipartimento di Matematica
Politecnico di Milano
Piazza L. da Vinci 32, I-20133 Milano, Italy
{yvesantonio.brandes,simona.perotto}@polimi.it

Abstract

In this contribution we consider cardiovascular hemodynamic modeling in patient-specific artery branches. To this aim, we first propose a procedure based on non-uniform rational basis splines (NURBS) to parametrize the artery volume which identifies the computational domain. Then, we adopt an isogeometric hierarchically reduced model which suitably combines separation of variables with a different discretization of the principal and of the secondary blood dynamics. This ensures the trade-off desired in numerical modeling between efficiency and accuracy, as shown by the good performances obtained in the numerical assessment of the last section.

1 Introduction

In recent decades, much progress has been made in research towards the coupling of medical imaging and computational fluid dynamics to study cardiovascular diseases [24]. The methods developed provide powerful tools to investigate the mechanism of diseases and to design medical devices and therapeutic interventions. In this paper, we focus on coronary arteries, which represent a common site for atherosclerotic lesion development. Mechanical stresses resulting from intravascular pressure and flow may contribute to the pathogenesis of atherosclerosis. In particular, flow perturbations associated with a stenosis can modify the rate of plaque development, the direction of plaque extension and the composition itself of the plaque. A detailed hemodynamic evaluation of the disturbed flow and of the spatial and temporal flow distribution patterns may provide an additional insight to understand the progression of atherosclerosis and may have useful clinical value. Nevertheless, it is not trivial to measure local flow patterns and mechanical forces in vivo with a sufficient accuracy.

Computational models become a useful tool in this regard [9]. In particular, reduced models have been widely employed to contain the computational burden of standard

three-dimensional models, with the aim of ensuring a trade-off between accuracy and efficiency, for instance, in the prediction of benchmark quantities. In this work we focus on hierarchically reduced models [8, 18] to perform a preliminary analysis in cardiovascular hemodynamics in a patient-specific framework. A first attempt, limited to synthetic configurations, was carried out in [10]. In [16], the authors develop a specific formulation of the hierarchical reduction to deal with real geometries. However, the accuracy of the proposed method is shown to be lower than that of the approach in [10], especially in the presence of highly oscillatory flows.

In this paper, after setting an ad-hoc procedure to build a NURBS volume parametrization of patient-specific arterial branches, we consider the isogeometric version of the Hierarchical Model reduction, aka a HIgaMod reduction [19]. The main strength of this approach is the capability to include in the modeling, while solving problems defined in a one-dimensional (1D) domain, the transverse dynamics usually discarded by downscaled models [9]. HIgaMod reduction exploits the idea of combining separation of variables with a different numerical approximation, to take advantage from particular features of the problem at hand. In more detail, along the mainstream we exploit the high geometric efficiency and flexibility of an isogeometric approximation, ideal for dealing with patient-specific geometries. The transverse components are modeled by a suitable modal expansion. The rapid convergence of spectral approximations allows us to capture the important features of the transverse dynamics with a relatively low number of modes. This results in accurate approximations with a lower number of degrees of freedom compared with non-customized discretizations like classical finite element solvers. Moreover, the use of an isogeometric discretization along the main stream allows us to overcome the limits intrinsically related to a polar reference system [10]. The numerical investigation carried out in the last section confirms the good performance of HIgaMod reduction in terms of numerical reliability and efficiency, as well as when employed to estimate common features used to assess the severity of stenotic lesions, such as the Fractional Flow Reserve index.

2 Reconstruction of patient-specific geometries

The reconstruction of a patient-specific geometry can be divided into four steps, namely, the image acquisition, the segmentation and the processing of the image, the reconstruction of the volume surface and the parametrization of the enclosed volume. In this work, we focus on the last step and, in particular, on the parametrization of segments of the Left and of the Right Coronary Arteries (the LCA and the RCA, respectively).

Figure 1 shows two X-ray images from patients suffering from a Coronary Artery (CA) disease¹, together with the corresponding reconstructed volume surfaces. The image segmentation and processing as well as the volume surface reconstruction are performed using the Vascular Modeling Toolkit (VMTK) [3]. The specific algorithms employed at this stage are not discussed here since beyond the goal of the paper. In

¹the dataset here analyzed is publicly available in the Dropbox repository <https://www.dropbox.com/sh/ytn5g5idp507j4k/AAAjQ0e-Zu9kZGiSH-Zx14Boa?dl=0>

the sequel, we propose a new procedure to parametrize the volume enclosed by these surfaces by resorting to non-uniform rational basis splines (NURBS) due to the great flexibility and the high accuracy provided by these functions [7, 12] and with a view to the model reduction performed in the next section.

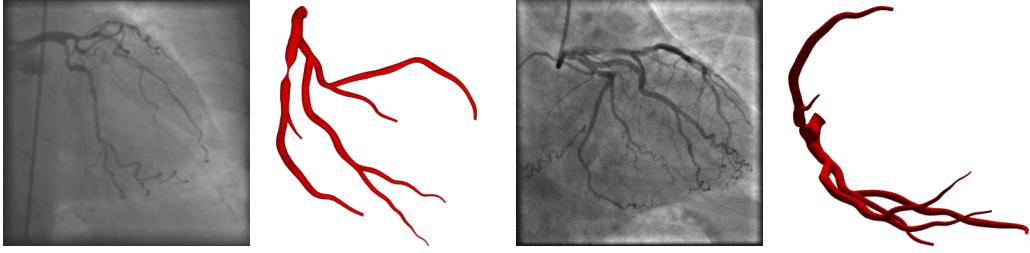


Figure 1: X-ray images of LCA and RCA trees (left panels) and corresponding volume surfaces (right panels) reconstructed with VMTK.

2.1 NURBS representation of swept volumes

The parametrization of a generic three-dimensional (3D) volume turns out to be a challenging task. In particular, it is not easy to find a unique method to successfully deal with any geometry. Here, we consider the special class of swept volumes, i.e., volumes which are obtained by moving through the space a two-dimensional (2D) shape (the cross section of the lumen), whose geometry may vary during the sweep [1]. We are interested in NURBS volumes, whose parametric representation is provided by

$$\mathbf{F}(r, s, t) = \sum_{i \in \mathcal{I}} \sum_{j \in \mathcal{J}} \sum_{k \in \mathcal{K}} R_{ijk}(r, s, t) w_{ijk} \mathbf{d}_{ijk} \quad \text{with } (r, s, t) \in \mathcal{D} = [0, 1]^3, \quad (1)$$

where the vector-valued coefficients $\mathbf{d}_{ijk} \in \mathbb{R}^3$ are the control points of the NURBS, while

$$R_{ijk}(r, s, t) = \frac{N_{i, \mathcal{R}}(r) N_{j, \mathcal{S}}(s) N_{k, \mathcal{T}}(t)}{\sum_{i' \in \mathcal{I}} \sum_{j' \in \mathcal{J}} \sum_{k' \in \mathcal{K}} w_{i'j'k'} N_{i', \mathcal{R}}(r) N_{j', \mathcal{S}}(s) N_{k', \mathcal{T}}(t)} \quad (2)$$

denotes the rational spline basis function associated with \mathbf{d}_{ijk} , $w_{ijk} \in \mathbb{R}$ being the corresponding weight [3]. Functions $N_{i, \mathcal{R}}$, $N_{j, \mathcal{S}}$, $N_{k, \mathcal{T}}$ ($N_{i', \mathcal{R}}$, $N_{j', \mathcal{S}}$, $N_{k', \mathcal{T}}$) are B-splines of a certain degree with respect to the knot vectors \mathcal{R} , \mathcal{S} and \mathcal{T} , respectively while the index sets for the control points, \mathcal{I} , \mathcal{J} , $\mathcal{K} \subset \mathbb{Z}$, depend on the knot sequences and on the degree of the B-splines [3].

The choice done for the domain \mathcal{D} is very straightforward but consistent with the purpose of the paper. Variable t is the sweep parameter and it is associated with the motion of the 2D shape, which is parametrized by r and s . More precisely, $\mathbf{F}(r, s, t^*)$ denotes the surface identified by the value $t^* \in [0, 1]$ of the sweep parameter, with $(r, s) \in [0, 1]^2$, while the curve $\mathbf{F}(r^\dagger, s^\dagger, t)$, describes the trajectory of the point $(r^\dagger, s^\dagger) \in [0, 1]^2$, when t varies in $[0, 1]$.

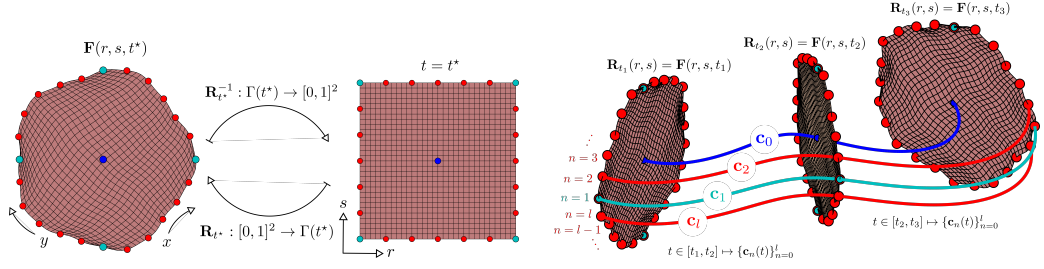


Figure 2: Maps \mathbf{R}_{t^*} and $\mathbf{R}_{t^*}^{-1}$ (left); tracking of some guiding curves during the sweeping process (right).

The two next sections are meant to formalize the approach adopted to provide a parametric representation as in (1) for a volume surface furnished by VMTK. Such a parametrization is not unique. In general, the weights, the control points, the degree and the knot vector of the B-splines can be varied to identify \mathbf{F} . Here, for the sake of simplicity, we assume that the control points \mathbf{d}_{ijk} constitute the only actual unknowns of the proposed parametrization, while setting the weights to 1, the B-spline degree to 3, and using uniformly distributed knots. Throughout the paper, we denote by $\mathbf{d} = (\mathbf{d}_{ijk})_{i \in \mathcal{I}, j \in \mathcal{J}, k \in \mathcal{K}}$ the vector gathering the points of the whole control net.

2.2 Boundary surfaces, guiding curves and reference shape

The parametrization procedure is initiated starting from the volume surface provided by VMTK. The first information we exploit is represented by the boundary surfaces, $\mathbf{F}_{\text{in}} = \mathbf{F}(r, s, 0)$ and $\mathbf{F}_{\text{out}} = \mathbf{F}(r, s, 1)$, which confine the volume of interest, Ω . These surfaces can be associated with the boundary nets, $\mathbf{d}_{\text{in}} = (\mathbf{d}_{ij \min \mathcal{K}})_{i \in \mathcal{I}, j \in \mathcal{J}}$ and $\mathbf{d}_{\text{out}} = (\mathbf{d}_{ij \max \mathcal{K}})_{i \in \mathcal{I}, j \in \mathcal{J}}$. When \mathbf{d}_{in} and \mathbf{d}_{out} are specified, we can remove the corresponding control points from the global set \mathbf{d} of unknowns. In hemodynamics, surfaces \mathbf{F}_{in} and \mathbf{F}_{out} coincide with the inflow and outflow profiles of the arterial segment and, in general, are known.

The second information to be specified is represented by a set of $(l + 1)$ functions, $\mathbf{c}_n : [0, 1] \rightarrow \mathbb{R}^3$ such that $t \mapsto \mathbf{c}_n(t)$ for $n = 0, \dots, l$, known as *guiding curves*. These curves work as tracks driving the motion of the 2D curve, $\Gamma = \Gamma(t)$, sweeping the volume Ω . Moreover, it is standard to consider a map $\mathbf{R}_t : \hat{\Gamma} \rightarrow \Gamma(t)$ with $(r, s) \rightarrow \Gamma(t) = \mathbf{R}_t(r, s) = \mathbf{F}(r, s, t)$, modifying a planar reference shape, $\hat{\Gamma}$, into the moving surface, $\Gamma(t)$. In Fig. 2, left we show an example of this map changing the unit square into $\Gamma(t^*) = \mathbf{F}(r, s, t^*)$. We observe that the Cartesian coordinates in $\hat{\Gamma}$ become curvilinear in $\Gamma(t^*)$, and that the four vertices of $\hat{\Gamma}$ split the boundary, $\partial\Gamma(t^*)$, of $\Gamma(t^*)$ into four portions. In general, the guiding curves, $\{\mathbf{c}_n(t)\}_{n=0}^l$, are associated with specific points, $R_t(\tilde{r}_n, \tilde{s}_n)$, images of the so-called *anchors*, $(\tilde{r}_n, \tilde{s}_n)$, of the reference shape, whose trajectory is controlled in the sweeping process. With reference to the parametrization of CA geometries, we select as parameters to be tracked the baricenter, (r^*, s^*) , of the artery cross section, and l points, $\{R_t(\tilde{r}_n, \tilde{s}_n)\}_{n=1}^l$, of the

boundary surface, so that the corresponding guiding curves, denoted by $\mathbf{c}^\star(t) = \mathbf{c}_0(t)$ and $\{\mathbf{c}_n(t)\}_{n=1}^l$, respectively identify the centerline of the artery (provided by VMTK) and l curves along the lateral surface, \mathbf{F}_{lat} , of the artery (see Fig. 2, right).

2.3 A variational approach

We build the NURBS representation for the volume Ω by minimizing an objective functional, \mathcal{L} , which combines a standard mismatch contribution with geometric constraints. In particular, we solve the minimization problem: find $\mathbf{d}^\star = \arg \min_{\mathbf{d}} \mathcal{L}(\mathbf{d})$, where

$$\begin{aligned} \mathcal{L}(\mathbf{d}) = & \underbrace{\sum_{n=0}^l \omega^{(n)} \int_0^1 \|\mathbf{F}(\tilde{r}_n, \tilde{s}_n, t) - \mathbf{c}_n(t)\|^2 dt}_{\text{mismatch term}} + \underbrace{\omega_O \int_{\mathcal{D}} \left\langle \mathbf{F}(r, s, t) - \mathbf{c}^\star(t), \frac{\partial_t \mathbf{c}^\star(t)}{\|\partial_t \mathbf{c}^\star(t)\|} \right\rangle^2 dr ds dt}_{\text{orthogonality constraint}} \\ & + \underbrace{\omega_R \int_{\mathcal{D}} \left\| \partial_t \mathbf{F}(r, s, t) \times \frac{\partial_t \mathbf{c}^\star(t)}{\|\partial_t \mathbf{c}^\star(t)\|} \right\|^2 dr ds dt}_{\text{rotation constraint}} + \underbrace{\omega_C \int_{\mathcal{D}} \|\partial_t \mathbf{F}(r, s, t)\|^2 dr ds dt}_{\text{regularity constraint}} \\ & + \underbrace{\sum_{n=1}^l \omega_S^{(n)} \int_0^1 \left[\langle \mathbf{F}(r^\star, s^\star, t) - \mathbf{F}(\tilde{r}_n, \tilde{s}_n, t), \mathbf{N}_n(t) \rangle - \nu_n \right]^2 dt}_{\text{shape constraint}}, \end{aligned} \quad (3)$$

with $(\tilde{r}_0, \tilde{s}_0) = (r^\star, s^\star)$, $\|\cdot\|$ the Euclidean norm, $\langle \cdot, \cdot \rangle$ the associated scalar product, $\partial_t \mathbf{c}^\star(t)$ the tangent vector associated with the centerline, $\partial_t \mathbf{F}(r, s, t)$ the tangent vector to the curve $\Gamma(t)$, \times the standard cross product, $\mathbf{N}_n(t) = \dot{\mathbf{c}}^\star(t) \times [\mathbf{c}^\star(t) + \mathbf{c}_n(t)] + \beta([\dot{\mathbf{c}}^\star(t) + \dot{\mathbf{c}}_n(t)] \times [\mathbf{c}^\star(t) + \mathbf{c}_n(t)])$ the unit normal vector to the so-called *ruled surface* [15], $\mathbf{q}(t, \beta) = (1-\beta)\mathbf{c}^\star(t) + \beta\mathbf{c}_n(t)$ with $\beta \in [0, 1]$, generated by the pair of guiding curves, $\mathbf{c}^\star(t)$ and $\mathbf{c}_n(t)$, ν_n the desired distance between the two points $\mathbf{F}(r^\star, s^\star, t)$ and $\mathbf{F}(\tilde{r}_n, \tilde{s}_n, t)$, and with $\omega^{(n)}$, ω_O , ω_R , ω_C , $\omega_S^{(n)}$ non-negative weights balancing the different contributions, with $\sum_{n=0}^l \omega^{(n)} + \omega_O + \omega_R + \omega_C + \sum_{n=1}^l \omega_S^{(n)} = 1$. Albeit beyond the purpose of this work, it can be proved the existence of at least a local minimum for the objective functional. Vector \mathbf{d}^\star will provide the control points in (1) identifying a possible parametric representation for Ω . Moreover, since \mathcal{L} is quadratic in \mathbf{d} , we are led to solve a linear system in the unknowns d_{ijk} .

Let us briefly comment now on the different contributions in (3), separately.

The *mismatch term* simply minimizes the distance between the guiding curves and the points of $\Gamma(t)$ associated with the anchors.

The *orthogonality constraint* imposes that the moving surface travels in the normal plane with respect to the centerline, $\mathbf{c}^\star(t)$, of the artery. A priori one should ensure the orthogonality of $\Gamma(t)$ with respect to all the guiding curves. Nevertheless, for $l > 1$, this is not trivial to be guaranteed even though possible (see, for instance, [1] where a weighted average of the guiding curves is adopted for this purpose).

The *rotation constraint* enforces any possible torsion of Γ around the centerline to be the closest as possible to zero during the whole sweeping procedure.

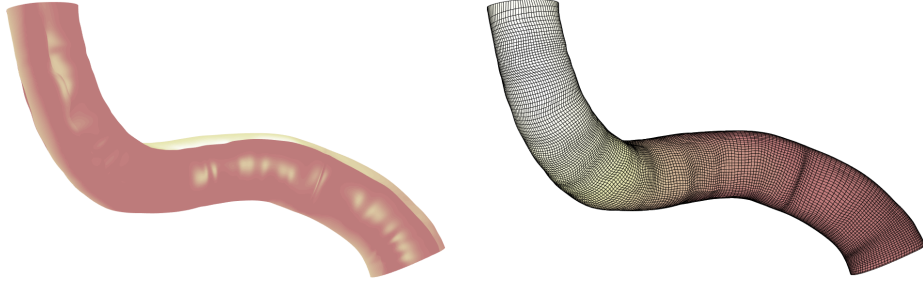


Figure 3: Selected branch of a CA network (left) and NURBS representation of the swept volume (right).

With a direct control on the derivative of the NURBS volume along t , the *regularity constraint* is meant to contain any possible oscillatory trend of Ω .

With the *shape constraint* we control the change of the moving shape during the sweeping, by imposing that the distance between the centerline of the artery and each of the guiding curves is equal to ν_n .

In Fig. 3, right we show the outcome of the procedure when applied to the VMTK volume surface in the left panel. As guiding curves we use the centerline of the artery and 24 curves equally spaced on the lateral surface. The maximum sampling distance is set to $4.1 \cdot 10^{-4}$ [m], to benefit of the high accuracy ensured by the VMTK segmentation algorithm. The weights in (3) are set to $\omega^{(n)} = \omega_O = \omega_S^{(n)} = 3\zeta$, $\omega_R = \omega_C = \zeta$, with $\zeta = 0.5/(3l + 4)$, while $\nu_n = 0$. All these values are preserved for the numerical assessment in Sect. 4.

3 HigaMod reduction for the Stokes equations

We identify the computational domain $\Omega \subset \mathbb{R}^3$ with the outcome of the parametrization procedure detailed in the previous section. In Ω we approximate the standard Stokes equations

$$\left\{ \begin{array}{ll} \partial_\tau \mathbf{u}(\mathbf{z}, \tau) + \nabla p(\mathbf{z}, \tau) - \nabla \cdot (2\nu \nabla_s \mathbf{u})(\mathbf{z}, \tau) = \mathbf{f}(\mathbf{z}, \tau) & \forall \mathbf{z} \in \Omega, \quad \tau \in I = (0, T] \\ \nabla \cdot \mathbf{u}(\mathbf{z}, \tau) = 0 & \forall \mathbf{z} \in \Omega, \quad \tau \in I \\ \mathbf{u}(\mathbf{z}, \tau) = \mathbf{g}(\mathbf{z}, \tau) & \forall \mathbf{z} \in \mathbf{F}_{\text{in}}, \quad \tau \in I \\ \mathbf{u}(\mathbf{z}, \tau) = \mathbf{0} & \forall \mathbf{z} \in \mathbf{F}_{\text{lat}}, \quad \tau \in I \\ (2\nu \nabla_s \mathbf{u} - p\mathbb{I})(\mathbf{z}, \tau) \mathbf{n}(\mathbf{z}) \cdot \mathbf{n}(\mathbf{z}) = 0 & \forall \mathbf{z} \in \mathbf{F}_{\text{out}}, \quad \tau \in I \\ \mathbf{u}(\mathbf{z}, 0) = \mathbf{u}_0(\mathbf{z}) & \forall \mathbf{z} \in \Omega, \end{array} \right. \quad (4)$$

where \mathbf{u} is the velocity field, p is the kinetic pressure, $\nu > 0$ is the kinematic viscosity, $\nabla_s \mathbf{u} = 0.5[\nabla \mathbf{u} + \nabla \mathbf{u}^T]$ is the symmetric gradient of the velocity representing the deformation of the velocity tensor, \mathbf{f} is the force per unit mass, \mathbf{g} is a given inflow profile, \mathbb{I} is the identity tensor, \mathbf{n} is the unit outward normal vector to the domain

boundary $\partial\Omega = \mathbf{F}_{\text{in}} \cup \mathbf{F}_{\text{out}} \cup \mathbf{F}_{\text{lat}}$, with \mathbf{F}_{in} , \mathbf{F}_{out} and \mathbf{F}_{lat} defined as in the previous section, and \mathbf{u}_0 is the assigned initial velocity. Problem (4) represents the so-called *full problem*.

The isogeometric hierarchical discretization applies to the weak form of the full problem. To simplify the notation, we assume $\mathbf{g}(\mathbf{z}, \tau) = 0$ in (4) and we denote by Γ_D the whole portion of $\partial\Omega$ where Dirichlet data are imposed, so that we have: for any $\tau \in I$, find $\mathbf{u} = \mathbf{u}(\tau) \in V = [H_{\Gamma_D}^1(\Omega)]^3$ and $p = p(\tau) \in Q = L^2(\Omega)$, such that

$$\begin{cases} \int_{\Omega} \partial_{\tau} \mathbf{u}(\tau) \cdot \mathbf{v} \, d\Omega + \int_{\Omega} 2\nu \nabla_s \mathbf{u}(\tau) : \nabla \mathbf{v} \, d\Omega - \int_{\Omega} p(\tau) \nabla \cdot \mathbf{v} \, d\Omega = \int_{\Omega} \mathbf{f}(\tau) \cdot \mathbf{v} \, d\Omega & \forall \mathbf{v} \in V, \\ \int_{\Omega} q \nabla \cdot \mathbf{u}(\tau) \, d\Omega = 0 & \forall q \in Q, \end{cases} \quad (5)$$

standard notation for function spaces being adopted. Problem (4) is completed with suitable assumptions on the data in order to ensure the well-posedness of formulation (5).

According to a HiMod reduction [8, 17, 18, 21], we introduce two different function spaces to model the blood flow along the main stream and the transverse direction. In particular, following [19], we employ an isogeometric approximation of the blood flow along the centerline, $\mathbf{c}^*(t)$, of Ω and a modal expansion to describe the dynamics parallel to the slices $\Gamma(t)$. Then, the computations are performed in a reference domain, $\hat{\Omega}$, related to the physical domain, Ω , by the invertible maps $\Psi : \Omega \rightarrow \hat{\Omega}$, with $\mathbf{z} = (x, y, z) \rightarrow \Psi(\mathbf{z}) = (\Psi_x(\mathbf{z}), \Psi_y(\mathbf{z}), \Psi_z(\mathbf{z}))$, and $\Phi : \hat{\Omega} \rightarrow \Omega$, with $\hat{\mathbf{z}} = (\hat{x}, \hat{y}, \hat{z}) \rightarrow \Phi(\hat{\mathbf{z}}) = (\Phi_{\hat{x}}(\hat{\mathbf{z}}), \Phi_{\hat{y}}(\hat{\mathbf{z}}), \Phi_{\hat{z}}(\hat{\mathbf{z}}))$. We assume that Ψ and Φ are differentiable with respect to \mathbf{z} and $\hat{\mathbf{z}}$, respectively. Moreover, with reference to the notation adopted in the previous section, we have that $\hat{\Omega} \equiv \mathcal{D}$, $\hat{\mathbf{z}} = (t, r, s)$, $\Phi \equiv \mathbf{F}$ and $\Psi \equiv \mathbf{F}^{-1}$.

Thus, the HIgaMod approximation for the velocity and the pressure in (4) is provided by suitable functions belonging to the reduced spaces

$$\begin{aligned} V_{m_u} &= \left\{ \mathbf{v}_{m_u}(\mathbf{z}) = \sum_{k=1}^{m_u} \sum_{j=1}^{N_{h,u}} \begin{bmatrix} v_{x,k,j} \\ v_{y,k,j} \\ v_{z,k,j} \end{bmatrix} \hat{R}_{q_u,j}(\Psi_x(\mathbf{z})) \hat{\phi}_{u,k}(\Psi_y(\mathbf{z}), \Psi_z(\mathbf{z})) \right\}, \\ Q_{m_p} &= \left\{ p_{m_p}(\mathbf{z}) = \sum_{w=1}^{m_p} \sum_{i=1}^{N_{h,p}} p_{w,i} \hat{R}_{q_p,i}(\Psi_x(\mathbf{z})) \hat{\phi}_{p,w}(\Psi_y(\mathbf{z}), \Psi_z(\mathbf{z})) \right\}, \end{aligned}$$

respectively, satisfying (5) after choosing $\mathbf{v} = \hat{R}_{q_u,b}(\Psi_x(\mathbf{z})) \hat{\phi}_{u,c}(\Psi_y(\mathbf{z}), \Psi_z(\mathbf{z}))$ and $q = \hat{R}_{q_p,e}(\Psi_x(\mathbf{z})) \hat{\phi}_{p,f}(\Psi_y(\mathbf{z}), \Psi_z(\mathbf{z}))$. Here, functions $\{\hat{R}_{q_u,b}\}_{b=1}^{N_{h,u}}$, $\{\hat{R}_{q_p,e}\}_{e=1}^{N_{h,p}}$ denote the NURBS of degree q_u and q_p , respectively defined in the interval $[0, 1]$ and employed to discretize \mathbf{u} and p along the centerline, while functions $\{\hat{\phi}_{u,c}\}_{c=1}^{m_u}$, $\{\hat{\phi}_{p,f}\}_{f=1}^{m_p}$ represent the modal basis adopted to model the transverse behaviour of the velocity and of the pressure, respectively. NURBS $\hat{R}_{q_u,b}$ and $\hat{R}_{q_p,e}$ have to include the boundary conditions on \mathbf{F}_{in} and \mathbf{F}_{out} . Functions $\hat{\phi}_{u,c}$ and $\hat{\phi}_{p,f}$ are demanded to be orthonormal with respect to the $L^2(\hat{\Gamma})$ -scalar product, with $\hat{\Gamma} = (0, 1)^2$. Moreover, following [2], we adopt *educated* modal bases which automatically include the boundary conditions assigned on \mathbf{F}_{lat} in an

essential way. This is achieved by solving an auxiliary (2D) Sturm-Liouville Eigenvalue (SLE) problem, $\mathcal{L}\varphi = \lambda\varphi$, in $\hat{\Gamma}$ completed with the desired boundary data on $\partial\hat{\Gamma}$. In particular, we choose $\mathcal{L} = \Delta$ for both the bases and we assign homogeneous Dirichlet and homogeneous Neumann boundary data for the velocity and for the pressure, respectively to impose the no-slip condition for \mathbf{u} and free pressure along the lateral wall of the artery. Additionally, thanks to the isogeometric approach, each 2D SLE problem reduces to two 1D SLE problems, so that functions $\hat{\varphi}_{u,c}(\Psi_y(\mathbf{z}), \Psi_z(\mathbf{z}))$ and $\hat{\varphi}_{p,f}(\Psi_y(\mathbf{z}), \Psi_z(\mathbf{z}))$ coincide with the products $\hat{\varphi}_{u,y,c}(\Psi_y(\mathbf{z})) \otimes \hat{\varphi}_{u,z,c}(\Psi_z(\mathbf{z}))$ and $\hat{\varphi}_{p,y,f}(\Psi_y(\mathbf{z})) \otimes \hat{\varphi}_{p,z,f}(\Psi_z(\mathbf{z}))$, with $\hat{\varphi}_{u,y,c}$, $\hat{\varphi}_{p,y,f}$ and $\hat{\varphi}_{u,z,c}$, $\hat{\varphi}_{p,z,f}$ solutions to the 1D SLE problems along the y - and the z -directions. This consideration allows us to skip all the issues intrinsically related to the employment of a polar coordinate system [10]. Finally, we remark that, a priori, one might adopt a different number of modes as well as different modal basis functions for each component of the velocity. The choice done above is meant to simplify the discussion.

Now, the HIgaMod approximation for problem (4) coincides with (5) formulated in the spaces V_{m_u} , Q_{m_p} , for given modal indices $m_u, m_p \in \mathbb{N}^+$. The reduced spaces for velocity and pressure are expected to fulfill an inf-sup condition [5]. While this issue has been largely investigated for isogeometric and spectral methods [4, 6], we are not aware of theoretical results dealing with hybrid methods merging both the techniques. Here, we adopt an empirical approach which proved to furnish reliable numerical results. In particular, given a certain degree $q_u \geq 2$ for the NURBS associated with the velocity and a certain modal index $m_u \geq 3$, the degree of NURBS $\{\hat{R}_{q_p,e}\}_{e=1}^{N_{h,p}}$ is set to $q_p = q_u - 1$, while the modal index for the pressure is chosen as $m_p = m_u - 2$. Additionally, an inter-element continuity at most $\mathbb{C}^{q_u-2}([0, 1])$ is assumed for both the NURBS bases. Modal indices set the accuracy of the HIgaMod discretization. In this work, we fix index m_u driven by a priori considerations. An adaptive selection of modal indices can be pursued, for instance, by generalizing the analysis developed in [20, 22]. From a computational viewpoint, HIgaMod approximation allows us to solve a system of coupled 1D problems instead of the full 3D one. The algebraic form of the semi-discrete HIgaMod approximation is

$$\begin{bmatrix} \mathbf{M}_x & \mathbf{0} & \mathbf{0} & \mathbf{0} \\ \mathbf{0} & \mathbf{M}_y & \mathbf{0} & \mathbf{0} \\ \mathbf{0} & \mathbf{0} & \mathbf{M}_z & \mathbf{0} \\ \mathbf{0} & \mathbf{0} & \mathbf{0} & \mathbf{0} \end{bmatrix} \begin{bmatrix} \dot{\mathbf{u}}_x \\ \dot{\mathbf{u}}_y \\ \dot{\mathbf{u}}_z \\ \dot{\mathbf{p}} \end{bmatrix} + \begin{bmatrix} \mathbf{A}_x & \mathbf{B}_{xy} & \mathbf{B}_{xz} & \mathbf{P}_x \\ \mathbf{B}_{yx} & \mathbf{A}_y & \mathbf{B}_{yz} & \mathbf{P}_y \\ \mathbf{B}_{zx} & \mathbf{B}_{zy} & \mathbf{A}_z & \mathbf{P}_z \\ \mathbf{Q}_x & \mathbf{Q}_y & \mathbf{Q}_z & \mathbf{0} \end{bmatrix} \begin{bmatrix} \mathbf{u}_x \\ \mathbf{u}_y \\ \mathbf{u}_z \\ \mathbf{p} \end{bmatrix} = \begin{bmatrix} \mathbf{F}_x \\ \mathbf{F}_y \\ \mathbf{F}_z \\ \mathbf{0} \end{bmatrix}, \quad (6)$$

with \mathbf{M}_s mass matrices, \mathbf{A}_s , \mathbf{B}_{st} and \mathbf{P}_s , \mathbf{Q}_s the matrices coupling the velocity components and velocity with pressure, respectively, \mathbf{F}_s the source term of the momentum equation and \mathbf{u}_s and \mathbf{p} the vectors collecting the HIgaMod (unknown) coefficients $u_{s,k,j}$ and $p_{w,i}$, for the velocity and for the pressure, respectively, being $s, t = x, y, z$, $k = 1, \dots, m_u$, $j = 1, \dots, N_{h,u}$, $w = 1, \dots, m_p$, $i = 1, \dots, N_{h,p}$. Then, each macroblock shares the pattern typical of the HiMod reduction applied to a scalar problem [18]. The time-dependence in (6) is finally tackled with the implicit Euler scheme.

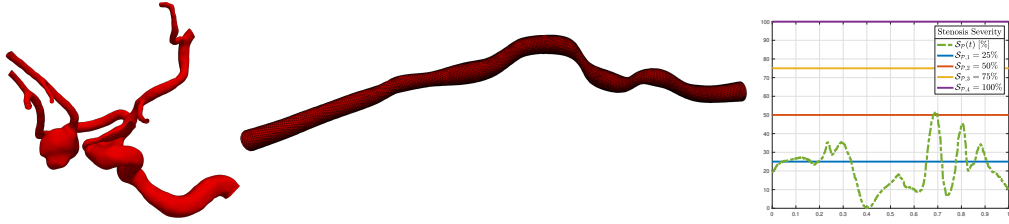


Figure 4: Test case 1: reconstruction of the original cerebrovascular network (left); branch representing the domain Ω (center); trend of the stenotic profile along the centerline (right).

4 Numerical assessment

In this section we investigate the reliability of the HIgaMod approximation on two patient-specific geometries. This investigation is performed by comparing HIgaMod with a standard finite element (FE) discretization, also to verify the efficiency characterizing the reduced modeling with respect to a full one. The second test case is meant to check the applicability of HIgamod in clinical analysis as well.

4.1 Test case 1: blood flow in a cerebrovascular arterial branch

We consider a segment of the cerebrovascular network shown in Fig. 4, left². The computational domain (shown in Fig. 4, center) is generated by resorting to the reconstruction procedure in Sect. 2. We evaluate the stenotic severity of the arterial branch by computing, for any \mathbf{z} along the centerline, the stenotic profile $\mathcal{S}_\varphi(\mathbf{z}) = 100 \cdot R_{\mathcal{D}}(\mathbf{z})/R_\varphi$ [%], where $R_{\mathcal{D}}(\mathbf{z})$ is the maximum inscribed distal (i.e., at the outflow) radius measured at \mathbf{z} , while R_φ measures the maximum inscribed proximal (i.e., at the inflow) radius. Fig. 4, right shows the profile of $\mathcal{S}_\varphi(\mathbf{z})$ compared with standard control values, $\mathcal{S}_{\varphi,1:4} = 25\%, 50\%, 75\%, 100\%$.

The problem data in (4) are set according to [13]. In particular, the density, ρ , and the dynamic viscosity, μ , of the fluid, such that $\nu = \mu/\rho$, are set to $1160 [kg/m^3]$ and to $4.5 \cdot 10^{-3} [Pa \cdot s]$, respectively to mimic the blood properties in medium size cerebral arteries. The velocity profile imposed at the inflow is set in the normal direction and with a constant value equal to the velocity expected in this region of the arterial tree, i.e., $\mathbf{g}(\mathbf{z}) = \bar{g}\mathbf{n}$ with $\bar{g} \approx 0.25 [m/s]$ and $\mathbf{z} \in \mathbf{F}_{in}$.

We approximate the solution to (4) by resorting both to a standard FE solver [11] and the HIgaMod discretization. The FE approximation is computed by resorting to a $\mathbb{P}_2 - \mathbb{P}_1$ basis associated with a 3D mesh consisting of 116104 elements, with a maximum diameter equal to 10^{-5} . Concerning the HIgaMod discretization, we adopt the empirical recipe provided in Sect. 3 to ensure the fulfillment of the inf-sup condition, by setting $q_u = 2$, $m_u = 5$, and by introducing a knot partition of $[0, 1]$ with a uniform

²the data used in this analysis comes from the ANEURYSK project and is publicly available in the repository <http://ecm2.mathcs.emory.edu/aneuriskweb/index>

step $h_x = 4 \cdot 10^{-2}$ for both NURBS $\{\hat{R}_{q_u,b}\}_{b=1}^{N_{h,u}}$ and $\{\hat{R}_{q_p,e}\}_{e=1}^{N_{h,p}}$. Fig. 5 compares the results provided by the FE and the HIgaMod approximations. From a qualitative point of view, the results are fully comparable. The reliability of the HIgaMod solution is confirmed also by quantifying the modeling error with respect to both the $L^2(\Omega)$ - and the $H^1(\Omega)$ -norms, being $\|\mathbf{u}_{\text{FE}} - \mathbf{u}_{m_u}\|_{L^2(\Omega)} = 1.4 \cdot 10^{-3}$, $\|p_{\text{FE}} - p_{m_p}\|_{L^2(\Omega)} = 2.7 \cdot 10^{-4}$ and $\|\mathbf{u}_{\text{FE}} - \mathbf{u}_{m_u}\|_{H^1(\Omega)} = 7.1 \cdot 10^{-2}$, $\|p_{\text{FE}} - p_{m_p}\|_{H^1(\Omega)} = 3.9 \cdot 10^{-2}$, respectively with \mathbf{u}_{FE} , p_{FE} the FE approximation. As expected, the gain provided by the reduced model in terms of efficiency is significant. Indeed, the HIgaMod approximation demands 109.732 [s] to be compared with 493.281 [s] required by the FE solver³. This is due to the lower number of HIgaMod degrees of freedom (DOFs) (i.e., 2100) with respect to the ones characterizing the FE solution (i.e., 563001).

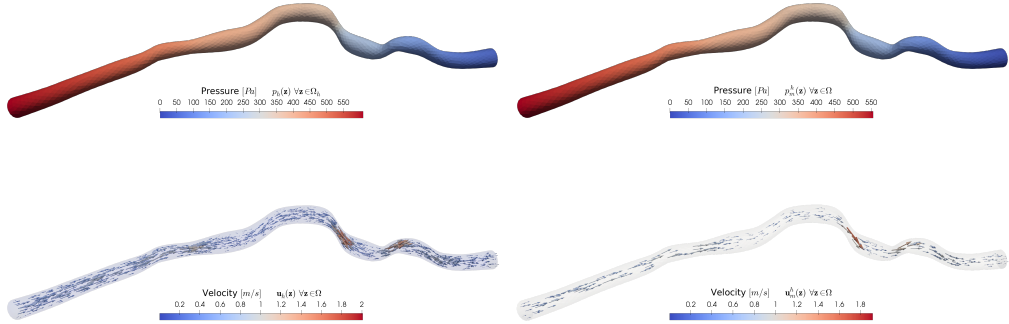


Figure 5: Test case 1: comparison between FE (left) and HIgaMod (right) approximations.

4.2 Test case 2: a stenotic lesion in a coronary artery

The reliability of HIgaMod in clinical practice is verified by extracting a portion of the coronary artery network both from a healthy (the control study) person and from a patient suffering from a severe stenotic lesion (see the left panels in Fig. 1). The volume parametrization of the stenotic artery turns out to be particularly challenging. Indeed, it exhibits some rotations and oscillations moving along the centerline. Despite that, it succeeds in detecting the features of the domain relevant for the simulation. The first two panels in Fig. 6 display the stenotic severity along the centerline both for the healthy ($\mathcal{S}_p^{(h)}(\mathbf{z})$) and for the stenotic ($\mathcal{S}_p^{(s)}(\mathbf{z})$) patient, still compared with reference control values. The criticality of the stenosis is highlighted by the trend of $\mathcal{S}_p^{(s)}$ in the second panel.

The data in (4) are chosen following [13], with a blood density, ρ , and dynamic viscosity, μ , set to $1060 [kg/m^3]$ and $5 \cdot 10^{-3} [Pa \cdot s]$, respectively to simulate the blood properties in large size coronary arteries. As in the previous test case, we impose at

³the computations have been run on a personal computer with a 2.2 GHz 6-Core Intel Core i7 processor (CPU 8750H) and 16 GB 2400 MHz LPDDR4 SDRAM.

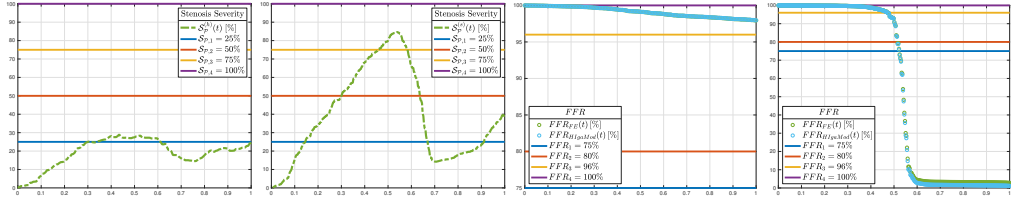


Figure 6: Test case 2: trend of the stenotic profile and of the FFR index along the centerline for the control study case (first and third panel) and for the sick patient (second and fourth panel).

the inflow a velocity profile in the normal direction and with a constant value, being $\mathbf{g}(\mathbf{z}) = \bar{g}\mathbf{n}$ with $\bar{g} \approx 0.1 [m/s]$ and $\mathbf{z} \in \mathbf{F}_{in}$.

We start by considering the blood flow modeling in the healthy branch. For the sake of comparison, we resort to a $\mathbb{P}_2 - \mathbb{P}_1$ FE discretization on a 3D mesh consisting of 72630 tetrahedra [11], with a maximum diameter equal to 10^{-5} , and to a HIgaMod discretization based on a knot partition of $[0, 1]$ with a uniform step, $h_x = 2 \cdot 10^{-2}$, for the NURBS associated both with the velocity and the pressure, and on the values $q_u = 2$ and $m_u = 7$. Figure 7 shows the pressure and the velocity trend for both the approximations. The matching is good, with slight differences in the pressure distribution towards the outflow section.

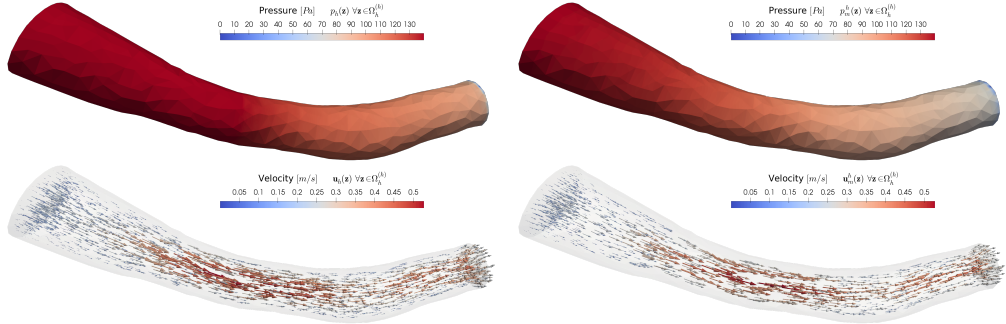


Figure 7: Test case 2, healthy patient: comparison between FE (left) and HIgaMod (right) approximations.

We consider now the stenotic patient. The reference $\mathbb{P}_2 - \mathbb{P}_1$ FE solution is computed on a mesh constituted by 145328 elements, and exhibiting a strong refinement in correspondence with the stenosis [11]. As far as the HIgaMod discretization is concerned, we set $m_u = 9$, $q_u = 3$ and we adopt a uniform knot partition of $[0, 1]$ with step $h_x = 5 \cdot 10^{-3}$ to define the NURBS functions $\{\hat{R}_{q_u, b}\}_{b=1}^{N_{h,u}}$ and $\{\hat{R}_{q_p, e}\}_{e=1}^{N_{h,p}}$. We relax the inter-element regularity by decreasing it to C^{q_u-3} . The locally refined mesh used for the FE simulation as well as the high order HIgaMod discretization combined with the relaxed inter-element continuity have proved to be necessary to deal with the steep gradients characterizing the velocity in the stenotic region and to avoid

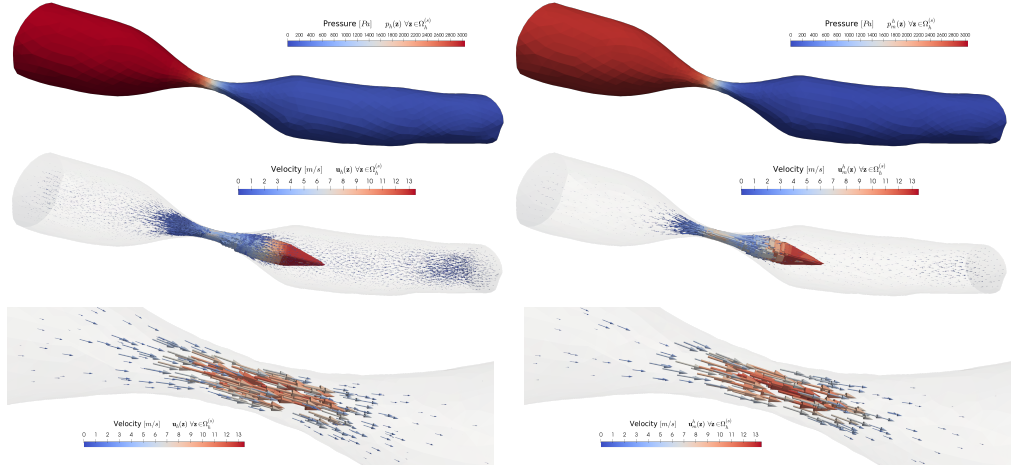


Figure 8: Test case 2, stenotic patient: comparison between FE (left) and HIgaMod (right) approximations.

the generation of spurious oscillations. Figure 8 gathers the pressure and the velocity yielded by the two discretizations. The reliability of HIgaMod is confirmed also for this challenging geometric configuration. Both p and \mathbf{u} are correctly described despite the severe stenotic area which strongly influences the local blood dynamics. The accuracy of the HIgaMod approximation is quantitatively corroborated by the L^2 - and by the H^1 -norm of the modeling error computed with respect to the FE approximation, $(\mathbf{u}_{FE}, p_{FE})$, being $\|\mathbf{u}_{FE} - \mathbf{u}_{m_u}\|_{L^2(\Omega)} = 1.2 \cdot 10^{-3}$, $\|p_{FE} - p_{m_p}\|_{L^2(\Omega)} = 9.7 \cdot 10^{-3}$ and $\|\mathbf{u}_{FE} - \mathbf{u}_{m_u}\|_{H^1(\Omega)} = 4.4 \cdot 10^{-2}$, $\|p_{FE} - p_{m_p}\|_{H^1(\Omega)} = 8.5 \cdot 10^{-2}$, respectively. The gain in terms of computational time provided by HIgaMod is remarkable, the HIgaMod discretization demanding about a quarter of the time required by the FE solver (153.334 [s] for HIgaMod to be compared with 646.081 [s] for FE).

We now move to the clinical investigation. In particular, we focus on the numerical computation of the Fractional Flow Reserve (FFR) index. FFR is used in coronary catheterization to measure pressure differences across a coronary artery stenosis to determine the likelihood that the stenosis impedes oxygen delivery to the heart muscle (myocardial ischemia). More rigorously, FFR is defined as the pressure after (distal to) a stenosis relative to the pressure before (proximal to) the stenosis. In clinical practice, patients with FFR values close to the treatment threshold (0.81 – 0.85) have a higher likelihood of future major adverse cardiac events when compared with patients with a near normal FFR value (0.96–1.0) [14]. To reliably exclude the presence of functionally significant stenoses, a threshold equal to 0.80 is routinely used to increase measurement sensitivity. Here we have computed as possible estimate for the FFR index the ratio between the pressure along the centerline and the pressure at the inflow, by modeling the pressure both with the FE and the HIgaMod approximations. The two last panels in Fig. 6 show the trend of this ratio for the healthy and for the stenotic patients. The two methods predict essentially the same index variation for the control subject, being

$FFR_{FE}(t) \geq 97.94\%$ for the FE solver and $FFR_{HIgaMod}(t) \geq 97.96\%$ for the HIgaMod approximation, with $t \in [0, 1]$. This patient clearly belongs to a risk-free zone in the reference spectrum according to both the models. On the contrary, a slight mismatch can be appreciated when comparing the FFR evolution along the centerline of the ill patient, although both the models detect the sharp fall of the pressure due to the severe arterial occlusion (the stenotic profile reaches approximately 85% in a neighborhood of $t = 0.53$). In particular, the location along the centerline where the critical values $FFR_1 = 75\%$ and $FFR_2 = 80\%$ are reached coincide with $t_{FE,1} = 0.5149$ and $t_{FE,2} = 0.5223$ with the FE solver and with $t_{HIgaMod,1} = 0.5153$ and $t_{HIgaMod,2} = 0.5229$ for the HIgaMod solver. These results show that both solvers identify this patient with a high risk profile.

The last results are very promising, although preliminary. They show that HIgaMod reduction allows us to reach a level of clinical accuracy fully comparable with the one provided by the full FE solver, while ensuring a remarkable reduction in computational costs, here understood in terms of computational time, number of DOFs and memory requirement.

As a possible follow-up of this work, we cite the extension of the approach here proposed to an arterial network, the introduction of simplified fluid-structure models to include the effect of the arterial wall and the generalization of the HIgaMod discretization to a parameter dependent setting to properly include patient data.

Acknowledgments

The authors would like to thank Riccardo Segliani who collaborated in the development of the code for volume parametrization [23], and Professor Hiroshi Suito for the helpful discussion on clinical practice. The financial support of INdAM-GNCS Project "Advanced Intrusive and Non-Intrusive Model Order Reduction Techniques and Applications" is also gratefully acknowledged.

References

- [1] Aigner, M., Heinrich, C., Jüttler, B., Pilgerstorfer, E., Simeon, B. and Vuong, A.V.. Swept Volume Parameterization for Isogeometric Analysis. In *Mathematics of Surfaces XIII*; Hancock, E.R., Martin, R.R., Sabin, M.A., Eds., Springer, Berlin, Germany, 2009; pp. 19–44.
- [2] Aletti, M.C., Perotto, S. and Veneziani, A.. HiMod Reduction of Advection–Diffusion–Reaction Problems with General Boundary Conditions. *J. Sci. Comput.* **2018**, 76, 89–119.
- [3] Antiga, L., Piccinelli, M., Botti, L., Ene-Iordache, B., Remuzzi, A. and Steinman, D.A.. An image-based modeling framework for patient-specific computational hemodynamics. *Med. Biol. Eng. Comput.* **2008**, 46, 1097–1112.

- [4] Bazilevs, Y., Beirão da Veiga, L., Cottrell, J.A., Hughes, T.J.R. and Sangalli, G.. Isogeometric analysis: approximation, stability and error estimates for h -refined meshes. *Math. Models Methods Appl. Sci.* **2006**, 16(7), 1031–1090.
- [5] Boffi, D., Brezzi, F. and Fortin, M.. *Mixed Finite Element Methods and Applications*. Springer-Verlag, Berlin Heidelberg, 2013.
- [6] Canuto, C., Hussaini, M.Y., Quarteroni, A. and Zang, T.A.. *Spectral Methods-Fundamentals in Single Domains*, Scientific Computation. Springer-Verlag, Berlin Heidelberg, 2006.
- [7] Cottrell, J.A., Hughes, T.J.R. and Bazilevs, Y.. *Isogeometric Analysis. Toward Integration of CAD and FEA*. John Wiley & Sons, Ltd., Chichester, 2009.
- [8] Ern, A., Perotto, S. and Veneziani, A.. Hierarchical model reduction for advection-diffusion-reaction problems. In *Numerical Mathematics and Advanced Applications*; Kunish, K., Günther, O., Steinbach, O., Eds., Springer, Berlin, Heidelberg, Germany, 2008; pp. 703–710.
- [9] *Cardiovascular Mathematics, Modeling, Simulation and Applications*. Series: *MS&A*, Vol. 1; Formaggia, L., Quarteroni, A. and Veneziani, A., Eds., Springer-Verlag, Berlin, Heidelberg, 2009.
- [10] Guzzetti, S., Perotto, S. and Veneziani, A.. Hierarchical model reduction for incompressible fluids in pipes. *Int. J. Numer. Methods Eng.* **2018**, 114, 469–500.
- [11] Hecht, F.. New development in FreeFem++. *J. Numer. Math.* **2012**, 20(3?4), 251–265.
- [12] Hughes, T.J.R., Cottrell, J.A. and Bazilevs, Y.. Isogeometric analysis: CAD, finite elements, NURBS, exact geometry and mesh refinement. *Comput. Methods Appl. Mech. Eng.* **2005**, 194, 4135–4195.
- [13] Huo, Y., Wischgoll, T. and Kassab, S.G.. Flow patterns in three-dimensional porcine epicardial coronary arterial tree. *Am. J. Physiol. Heart Circ. Physiol.* **2007**, 293, H2959–H2970.
- [14] Johnson, N.P., Toth, G.G., Lai, D., Zhu, H., Acar, G., Agostoni, P., et al. Prognostic value of Fractional Flow Reserve: linking physiologic severity to clinical outcomes. *J. Am. Coll. Cardiol.* **2014**, 64, 1641–1654.
- [15] Piegl, L.A. and Tiller, W.. *The NURBS Book*. Springer-Verlag, New York, NY, USA, 1996.
- [16] Mansilla Alvarez, L., Blanco, P., Bulant, C., Dari, E., Veneziani, A. and Feijóo, R.. Transversally enriched pipe element method (TEPEM): an effective numerical approach for blood flow modeling. *Int. J. Numer. Methods Biomed. Eng.* **2017**, 33(4), e02808, 24 pp.

- [17] Perotto, S.. A survey of hierarchical model (Hi-Mod) reduction methods for elliptic problems. In *Numerical Simulations of Coupled Problems in Engineering*; Series: *Computational Methods in Applied Sciences*, Vol. **33**; Idelsohn, S.R., Ed., Springer, 2014; pp. 217–241.
- [18] Perotto, S., Ern, A. and Veneziani, A.. Hierarchical local model reduction for elliptic problems: a domain decomposition approach. *Multiscale Model Simul.* **2010**, 8(4), 1102–1127.
- [19] Perotto, S., Reali, A., Rusconi, P. and Veneziani, A.. HIGAMod: A Hierarchical IsoGeometric Approach for MODEL reduction in curved pipes. *Comput. & Fluids* **2017**, 142, 21–29.
- [20] Perotto, S. and Veneziani, A.. Coupled model and grid adaptivity in hierarchical reduction of elliptic problems. *J. Sci. Comput.* **2014**, 60(3), 505–536.
- [21] Perotto, S. and Zilio, A.. Hierarchical model reduction: three different approaches. In *Numerical Mathematics and Advanced Applications*; Cangiani, A., Davidchack, R., Georgoulis, E., Gorban, A., Levesley, J., Tretyakov, M., Eds., Springer, Berlin, Heidelberg, Germany, 2011; pp. 851–859.
- [22] Perotto, S. and Zilio, A.. Space-time adaptive hierarchical model reduction for parabolic equations. *Adv. Model. Simul. Eng. Sci.* **2015**, 2(25), 1–45.
- [23] Segliani, R.. Optimal Reconstruction of Patient-Specific Geometries. Master Degree Thesis in Automation and Control Engineering, Politecnico di Milano, a.y. 2017-2018.
- [24] Villines, T.C.. Can CT-derived FFR better inform clinical decision-making and improve outcomes in stable ischaemic heart disease? *European Heart Journal* **2018**, 39, 3712–3714.

MOX Technical Reports, last issues

Dipartimento di Matematica
Politecnico di Milano, Via Bonardi 9 - 20133 Milano (Italy)

- 14/2019** Antonietti, P.F.; Facciola, C.; Verani, M.
Mixed-primal Discontinuous Galerkin approximation of flows in fractured porous media on polygonal and polyhedral grids
- 09/2019** Antonietti, P.F.; Facciola, C.; Verani, M.
Unified analysis of Discontinuous Galerkin approximations of flows in fractured porous media on polygonal and polyhedral grids
- 10/2019** Abramowicz, K.; Pini, A.; Schelin, L.; Sjostedt de Luna, S.; Stamm, A.; Vantini, S.
Domain selection and family-wise error rate for functional data: a unified framework
- 11/2019** Benacchio, T.; Klein, R.
A semi-implicit compressible model for atmospheric flows with seamless access to soundproof and hydrostatic dynamics
- 12/2019** Capezza, C.; Lepore, A.; Menafoglio, A.; Palumbo, B.; Vantini, S.
Control charts for monitoring ship operating conditions and CO2 emissions based on scalar-on-function regression
- 13/2019** Manzoni, A.; Quarteroni, A.; Salsa, S.
A saddle point approach to an optimal boundary control problem for steady Navier-Stokes equations
- 08/2019** Prouse, G.; Stella, S.; Vergara, C.; Engelberger, S.; Trunfio, R.; Canevascini, R.; Quarteroni, A.
Computational analysis of turbulent haemodynamics in radiocephalic arteriovenous fistulas with different anastomotic angles
- 07/2019** Dal Santo, N.; Manzoni, A.
Hyper-reduced order models for parametrized unsteady Navier-Stokes equations on domains with variable shape
- 06/2019** Pagani, S.; Manzoni, A.; Carlberg, K.
Statistical closure modeling for reduced-order models of stationary systems by the ROMES method
- 05/2019** Gasperoni, F.; Ieva, F.; Paganoni, A.M.; Jackson, C.; Sharples, L.
Evaluating the effect of healthcare providers on the clinical path of Heart Failure patients through a novel semi-Markov multi-state model